metals

Article

Application of Damage Detection of Metal Structure Lamb Wave Modal Superposition Imaging Based on Scanning Laser Vibration Measurement

Ziping Wang [1,*], Bingqian Li [1], Hangrui Cui [1], Rahim Gorgin [1], Jian Li [1] and Yang Zhang [2]

[1] National Center for International Research on Structural Health Management of Critical Components, Faculty of Civil Engineering and Mechanics, Jiangsu University, Zhenjiang 212013, China; bingqianl6@gmail.com (B.L.); 2212123020@stmail.ujs.edu.cn (H.C.); rgorgin@ujs.edu.cn (R.G.); lj66@ujs.edu.cn (J.L.)
[2] Institute of Fluid-Flow Machinery, Polish Academy of Sciences, 80-231 Gdańsk, Poland; yzhang@imp.gda.pl
* Correspondence: wzp@ujs.edu.cn

Abstract: Metal structural plates are extensively used in various engineering structures due to their high strength, high-temperature resistance, toughness, and plasticity. However, they are susceptible to damage from external loads and impacts over time. The current Lamb wave detection methods suffer from dispersion and multimodal effects, leading to ineffective identification of damage information. In this paper, we investigate Lamb wave propagation in steel structure plates with flat-bottomed holes using a sinusoidal modulation five-peak wave signal. Finite element numerical models are developed, and an experimental platform is constructed using steel and aluminum boards. Experimental data is collected using a Scanning Laser Doppler Vibrometer (SLDV, PSV-500, Polytec Inc., Baden-Württemberg, German). The results demonstrate that, under the same frequency, the damage reflection energy for different modes is distinct. By fusing the data from the two modes, more accurate damage imaging results are obtained in the frequency-wavenumber (f-k) domain compared to single-mode imaging. Furthermore, experiments are conducted to locate damage in a steel board with a through hole and an aluminum plate with double flat-bottomed holes, confirming the feasibility of the proposed algorithm in isotropic plates.

Keywords: metal structure plate; f-k field; modal separation and stacking; damage detection; Scanning Laser Doppler Vibrometer

check for updates

Citation: Wang, Z.; Li, B.; Cui, H.; Gorgin, R.; Li, J.; Zhang, Y. Application of Damage Detection of Metal Structure Lamb Wave Modal Superposition Imaging Based on Scanning Laser Vibration Measurement. *Metals* **2023**, *13*, 1668. https://doi.org/10.3390/met13101668

Academic Editor: Andrea Di Schino

Received: 28 August 2023
Revised: 21 September 2023
Accepted: 26 September 2023
Published: 28 September 2023

1. Introduction

Steel plate structures, among the earliest engineering solutions, have retained their widespread appeal in the modern era. This enduring popularity can be attributed to a multitude of advantages, making them a preferred choice for a variety of applications. These benefits include their remarkable strength-to-weight ratio, rapid construction capabilities, and exceptional seismic resilience [1–3]. With rapid urbanization and the prominent position of total steel production in the global market, the advantages of metal plate structures, including their comprehensive economic benefits and earthquake resistance, have been increasingly recognized [4]. Nonetheless, despite these merits, steel plate structures are not immune to the effects of long-term service. Over time, they can suffer from a range of issues, including fatigue, spalling, and other forms of damage. Addressing these challenges effectively is paramount to ensuring the continued safety and functionality of these structures. In this pursuit, non-destructive testing methods based on ultrasonic guided waves have emerged as a highly promising avenue [5–7]. These methods leverage the unique properties of guided ultrasonic waves, allowing for the detection and assessment of damage without compromising the structural integrity of the material. And the approach provides engineers and inspectors with a powerful tool to monitor the health of steel plate structures over their operational lifespans, enabling timely maintenance and repairs to mitigate potential risks [8–11].

The dispersion equation of Lamb waves in isotropic plates and corresponding dispersion curves were first studied by Achenbach [12] and Graff [13]. In 1991, Alleyne [14] introduced a method for analyzing multi-mode transmission signals, demonstrating the effectiveness of the two-dimensional Fourier transform (2D FFT) in identifying and measuring single modes. In 2003, Benz [15] utilized time–frequency imaging technology to analyze the interaction between multi-mode Lamb waves and dispersion in grooved plates, enabling the localization of groove defects. In 2007, Ruzzene [16] successfully separated the direct signal and scattered signal of a single Lamb wave mode using filtering techniques in the *f*-*k* domain. In 2009, Wang [17] proposed a wave packet reconstruction method to address the issue of wave packet aliasing in Lamb wave damage imaging. Experimental results validated the effectiveness of this method in improving the accuracy of active Lamb wave damage imaging. In 2014, Tian [18] provided a comprehensive description of using 2D and three-dimensional (3D) FFT for analyzing wave motion theorem and modal filtering. Modal Lamb wave decomposition was achieved by employing a filtering window function in the spatial domain, and the validity of modal decomposition was confirmed through time-delay power spectrum analysis. In 2021, Saito [19] et al. investigated the dispersion relation of Lamb wave propagation in cross-laminated CFRP laminates, comparing a uniform single-layer model with a multilayer model. It was obtained that the velocities of the S0 modes were the same for all models in the low-frequency region, whereas in the high-frequency region, there was a difference between the velocities of the Lamb wave modes of the homogeneous model and the multilayer model. In 2022, Haywood [20] et al. used a new Legendre polynomial expansion method to significantly reduce the computational cost of dispersion curve solutions and used a Bayesian approach to determine the properties that control the propagation of Lamb waves at different angles in the plate.

In 2016, Golato [21] proposed a multimodal sparse reconstruction method for defect localization in thin plates by leveraging the sparsity of defects and the multimodality of Lamb wave propagation. In 2019, Yang [22] employed a laser Doppler vibrometer to collect time–space domain signals, which were then transformed into the *f*-*k* domain through 3D FFT. A specifically designed arc-like window function was utilized to extract the damage scattering wave of a single Lamb wave mode, and the phased array method was applied for damage localization. In 2020, Zhang [23] utilized a linear phased array imaging method in the *f*-*k* domain to achieve S_0 mode double damage imaging, which demonstrated higher resolution compared to the time domain full focus method (TFM). In the same year, Gorgin [24] proposed a procedure for damage identification and characterization based on the principal curvature of the first mode of the plate. This method exploited changes in the mode shape of the structure, caused by cracks or material degradation, for damage identification. In 2021, Wang [25] et al. used a linear piezoelectric ultrasound array approach to achieve damage localization in composite plates under variable environmental conditions, which is primarily based on a two-dimensional multi-signal classification algorithm and adaptive transducer array error calibration to enhance the beam directivity of the linear array. In 2022, Wang [26] developed a mode decomposition imaging (MDI) algorithm for detecting delamination defects in carbon fiber composite panels using air-coupled Lamb waves. This algorithm involved the process of mode decomposition and rotational scanning defect probability imaging and proved to be more suitable for analyzing nonlinear non-stationary leaky Lamb wave signals. Recently, our research group [27,28] investigated damage imaging using the common source method (CSM) in both the time domain and *f*-*k* domain imaging for phased arrays.

In conclusion, guided waves offer significant advantages in monitoring damage in plate structures. However, existing research has overlooked the sensitivity of different modes for damage identification, with most studies focusing on through-hole damage. Limited research has been conducted on detecting flat-bottomed hole damage resulting from impact. Therefore, building upon previous research, this study proposes the use of multiple modes for damage imaging by examining simulated and experimental damage scenarios involving prefabricated flat-bottomed holes. The experimental data were obtained using a Scanning Laser Doppler Vibrometer (SLDV). This approach thoughtfully considers the effects of different guided wave modes, and the imaging results of the various modalities are comprehensively weighted, thereby further enhancing damage imaging accuracy and addressing the limitations of traditional single-modal damage imaging methods.

2. The Principle of Sub-Modal Superposition Imaging in the *f*-*k* Domain

The principle of sub-modal superposition imaging in the *f*-*k* domain is based on two essential steps for modal separation. The first step involves converting the signal from the time domain to the *f*-*k* domain using a 3D FFT. The second step is to construct a 3D window function in the *f*-*k* domain to isolate a single-mode guided wave. In this paper, the analysis primarily focuses on the symmetrical mode S_0 and antisymmetrical mode A_0 modes as they are typically the predominant modes observed in ultrasonic Lamb waves at low frequencies. The separation of these two modes is accomplished by constructing suitable 3D window functions in the *f*-*k* domain. The window width of the 3D window function was chosen to be 200 (1/m), and the window was added to the 3D Fourier-transformed signal matrix to realize the separation of the single S_0 and A_0 modes.

Figure 1 illustrates the flow chart of the sub-modal stack imaging method in the *f*-*k* domain. This method constitutes a pivotal component of the research's overall strategy, offering a structured and comprehensive approach for detecting and imaging structural anomalies within thin plate structures. The journey commences with the establishment of either a simulation model or an experimental platform, a crucial decision point that underscores the versatility of this methodology. Whether through the meticulous construction of numerical simulations or hands-on experimentation in real-world settings, the acquisition of guided wave data stands as the foundational step in the process. Upon the acquisition of data, the next pivotal phase involves the transformation of this information into an *f*-*k* domain matrix, an operation facilitated by the 3D FFT. This transformation is pivotal as it allows for a shift from the time domain representation of data to a frequency-wavenumber domain, which can reveal nuanced information about wave behavior and propagation characteristics. Subsequent to this transformation, the data undergoes a process of windowing using a specifically constructed 3D window function. This critical step serves the purpose of modal separation, enabling the isolation of individual modal signals from the composite data. The successful separation of modes is fundamental to the precision and accuracy of subsequent analyses. With the isolated single modality in hand, the *f*-*k* domain imaging is executed. This phase represents the heart of the methodology, where the characteristics and behaviors of the guided waves are thoroughly examined within the *f*-*k* domain. Finally, the modal overlay imaging phase brings together the results obtained from different modalities. By fusing these diverse imaging outcomes, the research achieves a comprehensive and holistic view of the structural integrity and potential anomalies within the thin plate structure [29]. This final synthesis of information serves as a powerful tool for engineers and inspectors, enabling them to make informed decisions about maintenance and strategies.

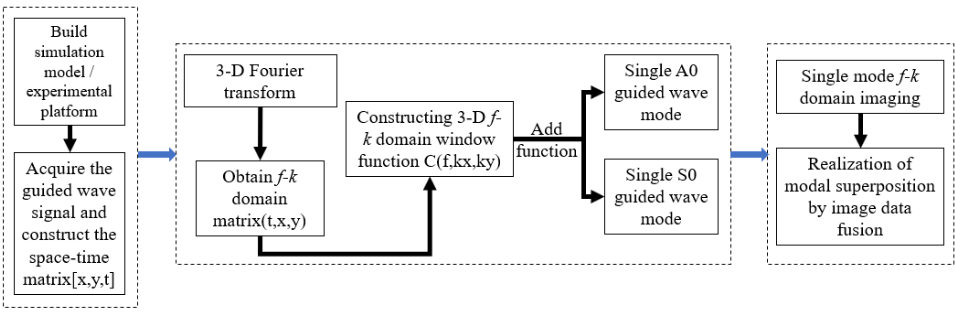

Figure 1. Flow chart of the method for sub-modal stacking imaging in the *f*-*k* domain.

2.1. 3D FFT

To analyze the wave field information for the propagation of Lamb waves in thin plates, the 3D FFT method [30] can be utilized. The 3D FFT of a 2D guided wave propagation problem is expressed by Equation (1),

$$A(f,k_x,k_y) = \int_{-\infty}^{\infty}\int_{-\infty}^{\infty}\int_{-\infty}^{\infty} a(t,x,y)e^{-i(2\pi ft - k_x x - k_y y)}d(t)d(x)d(y) \tag{1}$$

where k_x and k_y are wave number vectors along the x and y directions, respectively, t represents the variable in time, and f represents the variable in frequency. Its inverse transformation is as follows,

$$a(t,x,y) = \frac{1}{(2\pi)^2}\int_{-\infty}^{\infty}\int_{-\infty}^{\infty}\int_{-\infty}^{\infty} A(f,k_x,k_y)e^{i(2\pi ft - k_x x - k_y y)}d(f)d(k_x)d(k_y) \tag{2}$$

To convert the acquired time domain signal $a(x, y, t)$ to the f-k domain signal $A(f, k_x, k_y)$, the 3D FFT is applied. By selecting the desired quadrants in the f-k matrix obtained after the 3D FFT, the extraction of guided wave fields in different directions can be achieved. It is important to note that there exists a correspondence between the wave field information and the f-k matrix [31]. Finally, the time domain waveform can be obtained through the inverse 3D FFT.

2.2. 3D f-k Domain Window Function Design

To retain the desired frequency and wavenumber components, it is necessary to design a band-pass filter in the f-k space. As shown in Equation (3):

$$C(f,k_x,k_y) = c(f)c(f,k_x,k_y) \tag{3}$$

where $c(f)$ is a cosine window function, which can select different central frequencies in the frequency domain. $C(f, k_x, k_y)$ is the f-k domain window function for sub-modal imaging, as shown in the following formula:

$$c(f,k_x,k_y) = \begin{cases} \frac{1}{2}[1+\cos(\pi\frac{K_k(f,k_x,k_y)}{K_f})]\ if\ \ K_k(f,k_x,k_y) \le K_f \\ \quad\quad 0 \quad\quad\quad\quad\quad\quad else \end{cases} \tag{4}$$

where k_f is the designed window width, and $K_k(f, k_x, k_y)$ is as follows:

$$K_k(f,k_x,k_y) = |k| - k_{ref}(f) \tag{5}$$

where $|k| = \sqrt{k_x^2 + k_y^2}$, and $k_{ref}(f)$ is a reference signal, which can use the average value of the theoretical value or simulation or experimental results as a reference. So, the signal processing is as follows,

$$A_w(f,k_x,k_y) = A(f,k_x,k_y)C(f,k_x,k_y) \tag{6}$$

By applying Equation (4), the signals corresponding to various guided wave modes can be extracted. Then, the extracted signals can be analyzed to achieve damage imaging.

3. Numerical Simulation

3.1. Model Parameter Settings

The damaged metal plate model, as illustrated in Figure 2, presents geometric dimensions of 200 × 200 × 1 mm^3, reflecting a compact yet detailed experimental setup. Notably, a carefully induced flat-bottom hole damage is deliberately situated in the upper right corner, spanning a size of 6 mm with a depth of 0.7 mm. The coordinates of this flaw are precisely located at (60 mm, 40 mm). The red-shaded region within the diagram depicts a crucial area wherein guided wave signal data were meticulously scanned and received through the employment of a thoughtfully designed rectangular array. This scanning zone elegantly covers a span of 40 × 40 mm^2, and the deliberate choice of maintaining a 1 mm separation between individual array elements underscores the precision and granularity of the data collection process. For the purpose of excitation, a distinctive five-peak waveform signal, characterized by its center frequency of 250 kHz, was astutely selected. This choice aims to strike a balance between signal complexity and computational efficiency, enabling insightful analyses without overwhelming computational resources. Considering the efficiency of the computer and the correctness of the results, the meshing size was set to 0.2 mm for this paper. To ensure the fidelity of the obtained results, a meticulous approach was adopted to minimize unwanted boundary reflections. This entailed the application of a low reflection boundary condition meticulously implemented at the periphery of the simulation model. A noteworthy addition to this model is the implementation of a Rayleigh damping absorption layer, encompassing a width of 5 mm. This absorbing layer was strategically introduced to effectively mitigate wave reflections arising at the boundaries, a common concern in wave propagation simulations. Its careful integration reflects a commitment to producing accurate results by minimizing the influence of artificial reflections that could otherwise obscure the data interpretation.

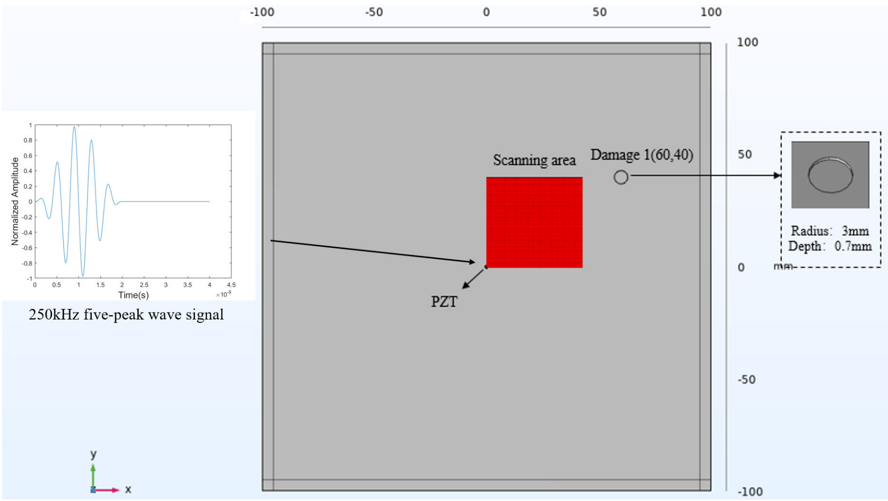

Figure 2. COMSOL model of a steel plate with flat-bottomed holes.

3.2. Simulation Results and Analysis of f-k Domain Sub-Modal Superposition Imaging

The intricate process of modal separation within the signal unfolded through the meticulous utilization of a purposefully constructed 3D window function, a cornerstone technique in this analysis. This window function efficiently disentangled the composite signal, enabling the extraction of singular mode reflection signals that hold pivotal insights into the structural dynamics under scrutiny. The paramount importance of this methodology lies in its capacity to dissect the complex signal into discernible components, enhancing the accuracy and depth of subsequent analyses. Figure 3a–c exemplify the outcome of this modal separation procedure, portraying time domain signals originating from an individual array unit and distinct A_0 and S_0 modes, each meticulously normalized for precise comparison. These visual representations distinctly underscore the effectiveness of the modal separation, as the different modes stand isolated, ready for focused scrutiny. A keen observer can readily discern the uniqueness of each mode and the absence of overlap, validating the efficacy of the applied modal separation technique. Figure 3d introduces us to the time domain waveform resulting from the deliberate removal of the direct wave. This step has proven pivotal in refining the subsequent analysis, isolating the reflections that arise from various sources and scattering phenomena. Figure 3e,f shine a spotlight on the intriguing reflection waves belonging to the A_0 and S_0 modes, respectively. It is noteworthy that the initial wave packet perceptibly corresponds to the scattering phenomena stemming from the existing damage. Subsequent wave packets, however, are intriguingly linked to boundary scattering, further illuminating the intricate interaction between guided waves and the structural boundaries.

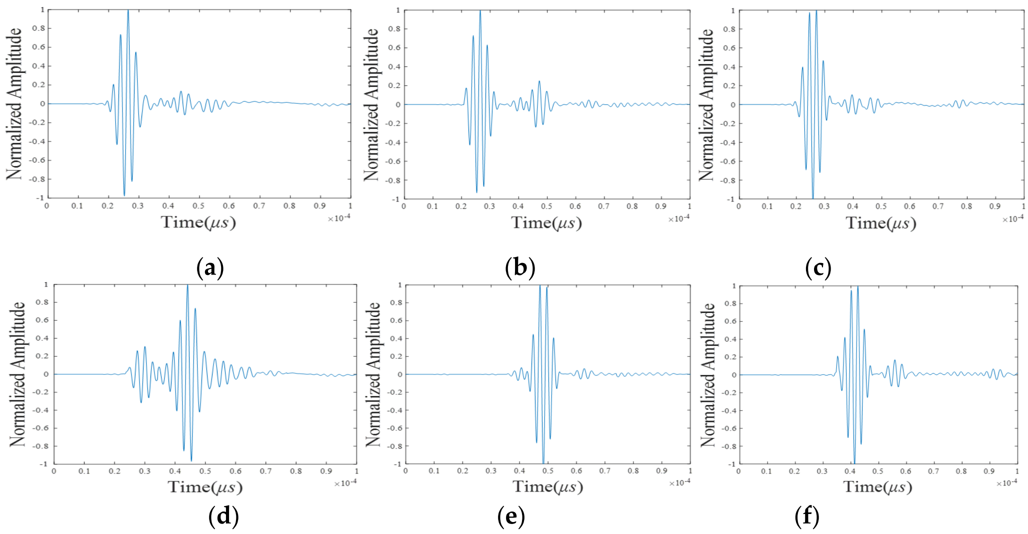

Figure 3. Waveform diagram of array element in time domain: (**a**) original waveform of an array element, (**b**) single A_0 modal, (**c**) single S_0 modal, (**d**) reflected waveform of an array element, (**e**) A_0 modal reflected waveform, (**f**) S_0 modal reflection waveform.

The imaging results in the *f*-*k* domain are presented in Figure 4, where the black circle represents the actual damage position. Figure 4a,b illustrate the *f*-*k* imaging results of the single A_0 and S_0 modes, respectively. Figure 4c–e display the imaging results in the *f*-*k* domain obtained using the amplitude stacking method, the amplitude stacking multiplication method, and the combined method of amplitude addition and multiplication. From the figure, it is evident that the combined method of amplitude stacking and multiplication achieves more effective damage localization compared to the amplitude stacking method alone. Additionally, the combined method exhibits a smaller and more accurate damage imaging area. In Figure 4e, the top left is the real damage and the bottom right is the artifact produced by the scattering of the wave as it approaches the damage.

By comparing the coordinates of the highest amplitude points in the images with the actual damage location, the following observations can be made: In the single A_0 modal image, the coordinates of the highest amplitude point are (62, 40), resulting in an error of 2 mm in relation to the actual damage location. In the single S_0 modal image, the coordinates of the highest amplitude point are (58, 41), resulting in an error of 2.23 mm in relation to the actual damage location. After numerical fusion processing, the coordinates of the highest amplitude point in the damage imaging with the amplitude stacking method are (61, 41), resulting in an error of 1.41 mm in relation to the actual damage location. The coordinates of the highest amplitude points obtained by the other two methods are (60, 40), with negligible error, indicating an accurate damage location.

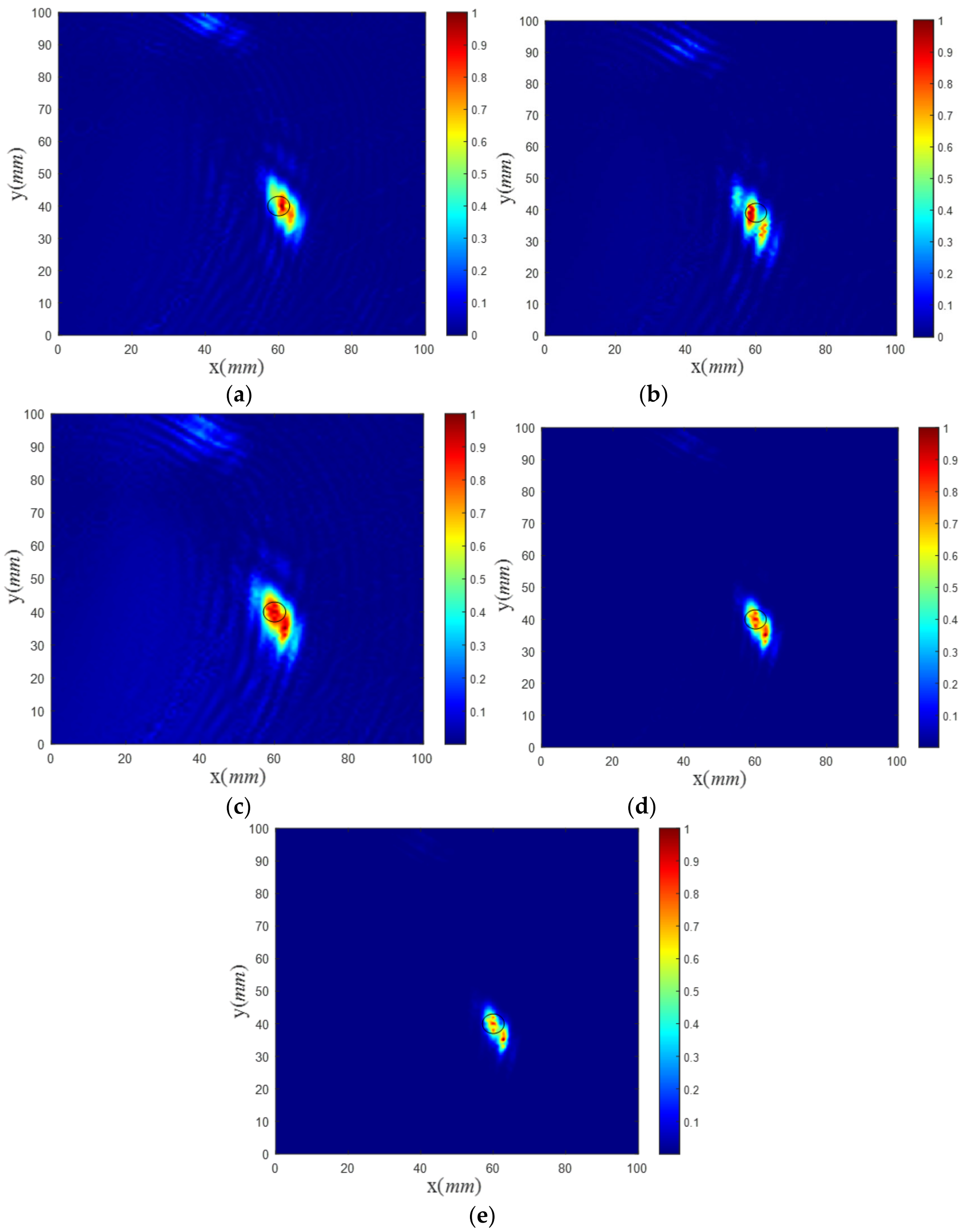

Figure 4. Imaging results in *f*-*k* domain: (**a**) single A_0 modal; (**b**) single S_0 modal; (**c**) S_0, A_0 modal amplitude stacking imaging results; (**d**) S_0, A_0 modal amplitude multiplication imaging results; (**e**) the combined imaging result of S_0 and A_0 modal amplitude.

4. *f*-*k* Domain Sub-Modal Superposition Imaging Experiment

4.1. Experimental Setup

The excitation position of the steel plate, the size of the damage, and the position parameters in the experiment are shown in Table 1. The steel plate selected for the experiment has dimensions of 800 × 800 × 1 mm^3. The experimental platform was shown in Figure 5. The excitation signal was generated by a signal generator with an amplitude of 5 V and a five-peak wave signal with a center frequency of 250 kHz, which was amplified by a power amplifier 20 times and then output by PZT. The vibration signals from the corresponding scanning area on the steel plate were collected using the SLDV. The size of the signal collection area was 70 × 70 mm, and the spacing between array elements was 1.4 mm.

Table 1. Parameter table of PZT and damage location in plate.

Test Subject	Size (mm)	PZT Location (mm)	Damage Center Location (mm)	Damage Diameter (mm)
Q235 steel plate	800 × 800 × 1	(0, 0)	(120, 120)	10

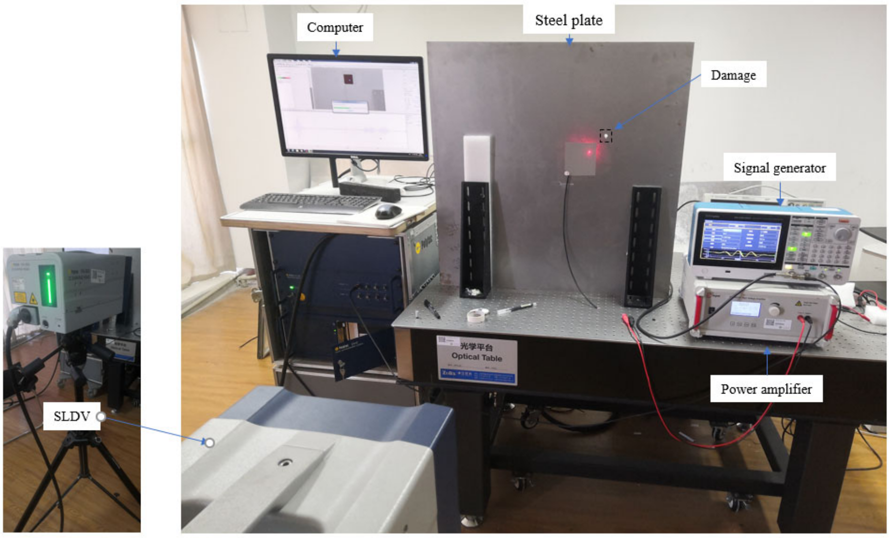

Figure 5. Schematic diagram of the isotropic steel plate sub-modal superposition imaging experimental platform.

4.2. Experimental Results and Analysis of f-k Domain Sub-Modal Stack Imaging

The achievement of modal separation in the signal processing methodology employed here was a crucial step in this study. This separation was made possible through the utilization of a specifically constructed 3D window function, which played a pivotal role in extracting individual modal reflection signals from the composite data. The effectiveness of this modal separation process is vividly illustrated in Figure 6a–c, where the time domain signals from an array unit are presented alongside the isolated A_0 and S_0 modes. These signals have been thoughtfully normalized for clarity, allowing for a clear visual distinction between the various modes. The results unequivocally demonstrate that the distinct modes have been successfully disentangled from the original signal, an achievement of paramount importance for accurate damage detection and localization. Figure 6d offers insight into the time domain waveform after the removal of the direct wave. This step is crucial in the signal processing pipeline as it allows researchers to focus exclusively on the reflected waves, which carry valuable information about the presence and characteristics of damage within the material. Figure 6e,f delve deeper into the reflection waves of the A_0 and S_0 modes, respectively. Within these figures, the temporal progression of the reflected waves is evident. The first discernible wave packet signifies damage scattering, a critical indicator of the structural anomaly under investigation. Subsequent wave packets, prominently visible in both A_0 and S_0 modes, correspond to boundary scattering phenomena. These multiple wave packets provide essential clues about the interactions occurring within the material, shedding light on not only the presence of damage but also its spatial distribution and potential boundaries or interfaces within the structure.

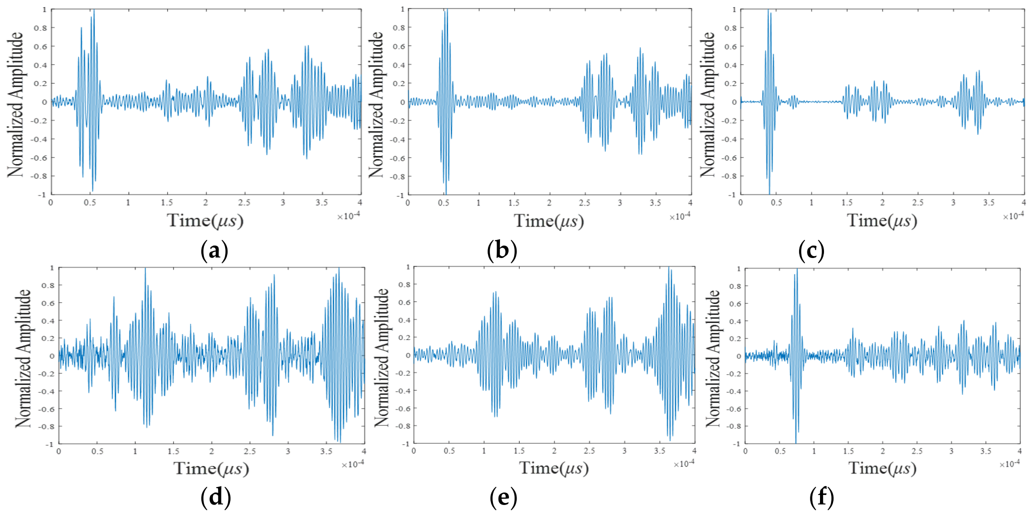

Figure 6. Waveform diagrams of array element in time domain: (**a**) original waveform of an array element, (**b**) single A_0 modal, (**c**) single S_0 modal, (**d**) reflected waveform of an array element, (**e**) A_0 modal reflected waveform, and (**f**) S_0 modal reflected waveform.

The imaging results in the *f*-*k* domain are shown in Figure 7. Figure 7a,b show the *f*-*k* imaging results of single A_0 and S_0 modes respectively. The damage range of S_0 mode imaging is larger than that of A_0 mode imaging range, and there are two darker positions with higher amplitudes and farther away from the actual damage. The overall error is large. The imaging results of different modalities are processed by numerical fusion. Figure 7c–e are the imaging results of the amplitude stacking method, the amplitude stacking multiplication method, and the combined method of the amplitude adding and multiplying in the *f*-*k* domain. Compared with the other two methods, the combined method of the amplitude adding and multiplying has higher accuracy for damage imaging.

By comparing the coordinates of the highest amplitude point in the images with the actual damage location, the following observations were made. In the single A_0 modal image, the coordinates of the highest amplitude point were found to be (122, 121), resulting in an error of 2.23 mm. In the single S_0 modal image, the coordinates of the highest amplitude point were (121, 121), resulting in an error of 1.41 mm. After numerical fusion processing, the coordinates of the highest point in the damage imaging using the amplitude stacking method were (121, 121), resulting in an error of 1.41 mm. In the other two methods of damage imaging, the coordinates of the highest point were (120, 120), with a negligible error, and the damage location was accurate. It is evident that the combined method of amplitude adding and multiplying has the best imaging effect, providing accurate damage location information with minimal error.

4.3. Experimental Results and Analysis of Aluminum Plate with Double Flat-Bottomed Holes

The experiment, conducted on the aluminum plate measuring 700 mm $\times$ 700 mm $\times$ 1 mm, was meticulously designed to provide valuable insights into the behavior of guided ultrasonic waves in the presence of intentional damage. Positioned at the center of the plate, with coordinates (0 mm, 0 mm) serving as the origin, were strategically placed PZT sensors. These sensors played a pivotal role in both exciting and capturing the responses of the guided waves within the plate. To create controlled damage scenarios, two flat-bottomed holes were precisely fashioned at coordinates (90 mm, 90 mm) and (100 mm, 50 mm) on the plate's surface. Each of these damage sites featured a 4 mm diameter and a depth of 0.7 mm ($\pm$0.03 mm), ensuring uniformity and precision in the experimental setup. The experimental setup meticulously adhered to the layout and configuration detailed in Section 4.1 of this study. Figure 8 shows the combined imaging result of S_0 and A_0 modal amplitudes with double flat- bottomed holes in aluminum plate by the original algorithm.

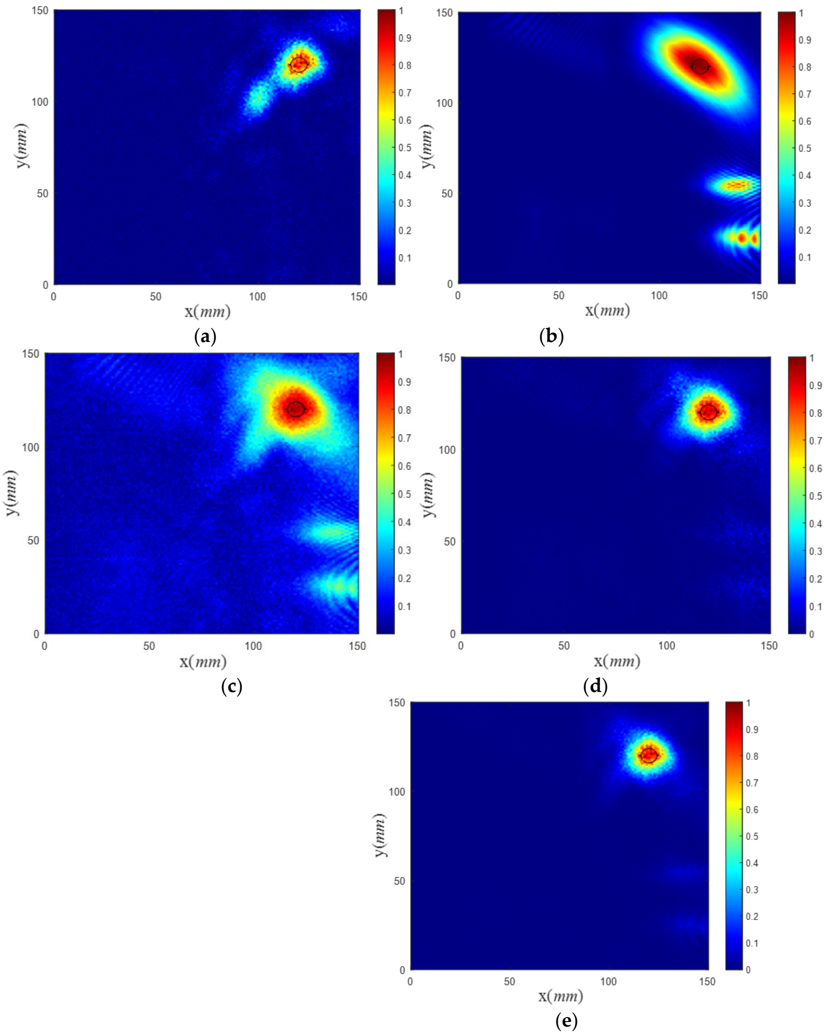

Figure 7. Imaging results in *f*-*k* domain: (**a**) single A_0 modal, (**b**) single S_0 modal, (**c**) S_0, A_0 modal amplitude stacking imaging results, (**d**) S_0, A_0 modal amplitude multiplication imaging results, and (**e**) the combined imaging result of S_0 and A_0 modal amplitudes.

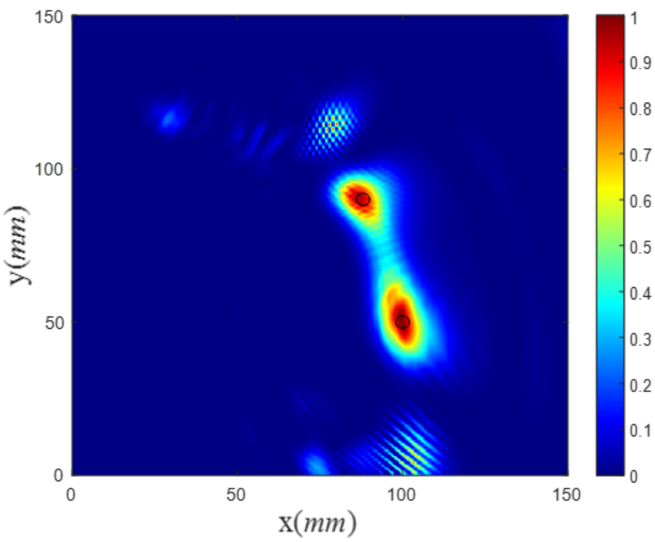

Figure 8. The combined imaging result of S_0 and A_0 modal amplitudes with aluminum plate.

As shown in Figure 8, this visualization offers a rich and multidimensional depiction of guided wave propagation behavior across various frequencies and wave numbers. Importantly, it serves as a powerful tool for delivering insights that might be elusive when relying solely on time domain signals. The significance of the frequency-wavenumber domain imaging approach cannot be overstated. It elegantly synthesizes information from multiple wave modes, providing a more comprehensive and accurate portrayal of damage localization. Intriguingly, the experiment's results yielded a crucial validation point when comparing the coordinates of the highest amplitude within this imaging composite with the actual damage locations. This alignment underscores the precision and reliability of the proposed methodology, reaffirming its potential as a robust technique for damage detection and localization in thin plate structures.

5. Conclusions

Through the construction of a finite element numerical model and the establishment of a corresponding damage detection experimental platform, the sub-modal damage imaging processing was conducted on signals obtained from simulations and experiments. The f-k domain modal imaging results demonstrate accurate identification of damage caused by flat-bottomed holes in metal structural plates and aluminum plates. Furthermore, after numerical fusion processing, the results reveal good agreement between the determined damage center and the actual damage center. By incorporating data fusion from two modalities instead of relying on a single mode, the imaging accuracy of damage is significantly improved, thus verifying the feasibility and practicality of the algorithm. This research contributes to addressing the challenges associated with modal separation of multimodal Lamb waves in sheet metal structures and the identification of multiple small areas of damage on the structure's surface.

Author Contributions: Conceptualization, Z.W.; Methodology, Z.W. and B.L.; Software, H.C.; Validation, R.G. and J.L.; Data curation, B.L.; Writing—original draft, Z.W. and B.L.; Writing—review & editing, R.G. and Y.Z. All authors have read and agreed to the published version of the manuscript.

Funding: This research was funded by the China Scholarship Council (No.202008320084, Ziping Wang), the National Natural Science Foundation of China (No.12072133 and No.11872191, Ziping Wang), the Foreign Expert Project of Chinese Ministry of Science Technology (DL2022014011L, Rahim Gorgin), and the Postgraduate Research & Practice Innovation Program of Jiangsu Province (KYCX22_3615, Hangrui Cui). Thanks to Yang Zhang for contacting European Cooperation in Science and Technology CA21155, CA18203 and providing relevant open source knowledge.

Data Availability Statement: The authors of this study were unable to find a valid data repository for the data produced in this study. But we can share the data as requested from the author.

Conflicts of Interest: The authors declare no conflict of interest regarding the publication of this paper.

References

1. Miki, C.; Homma, K.; Tominaga, T. High strength and high performance steels and their use in bridge structures. *J. Constr. Steel Res.* **2002**, *58*, 3–20. [CrossRef]
2. Yang, X.; Kersemans, M. Ultrasonic imaging of damage in plates in spectral ripple frequency domain. *Mech. Syst. Signal Process.* **2023**, *195*, 110312. [CrossRef]
3. Wald, F.; Da Silva, L.S.; Moore, D.B.; Lennon, T.; Chladna, M.; Santiago, A.; Beneš, M.; Borges, L. Experimental behaviour of a steel structure under natural fire. *Fire Saf. J.* **2006**, *41*, 509–522. [CrossRef]
4. Zhong, T.; He, B. Developing new-type light-gage steel structure in China. *Eng. Sci.* **2000**, *2*, 77–81.
5. Chang, H.Y.; Yuan, F.G. Visualization of hidden damage from scattered wavefield reconstructed using an integrated high-speed camera system. *Struct. Health Monit.* **2020**, *1*, 147592172094080. [CrossRef]
6. Sang, S.; Sandgren, E.; Wang, Z. Wave attenuation and negative refraction of elastic waves in a single-phase elastic metamaterial. *Acta Mech.* **2018**, *229*, 2561–2569. [CrossRef]
7. Chang, H.Y.; Yuan, F.G. Damage imaging in a stiffened curved composite sandwich panel with wavenumber index via Riesz transform. *Struct. Health Monit.* **2020**, *19*, 902–916. [CrossRef]
8. Jodhani, J.; Handa, A.; Gautam, A.; Ashwni; Rana, R. Ultrasonic non-destructive evaluation of composites: A review. *Mater. Today Proc.* **2023**, *78*, 627–632. [CrossRef]

9. Prasad, K.S.; Jombo, G.; Ismail, S.O.; Chen, Y.K.; Dhakal, H.N. Determination of acousto-ultrasonic wave propagation in an isotropic aluminium Al6082-T6 plate. *Researchsquare* **2023**, *preprint*. [CrossRef]
10. Foster, E.A.; Sweeney, N.E.; Nicolson, E.; Singh, J.; Rizwan, M.K.; Lines, D.; Pierce, G.; Mohseni, E.; Gachagan, A.; Tant, K.M.; et al. Thermal compensation of ultrasonic transmit and receive data for steel welded plates at the point of manufacture. *NDT E Int.* **2023**, *137*, 102812. [CrossRef]
11. Zitouni, I.; Rhimini, H.; Chouaf, A. Modeling the Propagation of Ultrasonic Guided Waves in a Composite Plate by a Spectral Approximation Method. *Eng. Trans.* **2023**, *71*, 213–227.
12. Mendelsohn, D.A.; Achenbach, J.D.; Keer, L.M. Scattering of Elastic-Waves by A Surface-Breaking Crack. *Wave Motion* **1980**, *3*, 277–292. [CrossRef]
13. Rokhlin, S.I.; Lewis, D.K.; Graff, K.F. Real-time study of frequency-dependence of attenuation and velocity of Ultrasonic-Waves during the curing reaction of epoxy-resin. J. *Acoust. Soc. Am.* **1986**, *6*, 1786–1793. [CrossRef]
14. Alleyne, D. A two-dimensional Fourier transform method for the measurement of propagating multimode signals. *J. Acoust. Soc. Am.* **1991**, *89*, 1159–1168. [CrossRef]
15. Benz, R.; Niethammer, M.; Hurlebaus, S.; Jacobs, L.J. Localization of notches with Lamb waves. *J. Acoust. Soc. Am.* **2003**, *114*, 677–685. [CrossRef] [PubMed]
16. Ruzzene, M. Frequency-wavenumber domain filtering for improved damage visualization. *Smart Mater. Struct.* **2007**, *16*, 2116. [CrossRef]
17. Wang, Q.; Yuan, S.F. Wave packet reconstruction method in active Lamb wave damage imaging monitoring. *Chin. J. Astronaut.* **2009**, *30*, 1207–1211.
18. Tian, Z.; Yu, L. Lamb wave frequency-wavenumber analysis and decompositio. *J. Intell. Mater. Syst. Struct.* **2014**, *25*, 1107–1123. [CrossRef]
19. Saito, O.; Yu, F.M.; Okabe, Y. Dispersion relation of Lamb waves in cross-ply composite laminates using multi-layered models. *Compos. Struct.* **2021**, *264*, 113691. [CrossRef]
20. Haywood-Alexander, M.; Dervilis, N.; Worden, K.; Rogers, T.J. A Bayesian Approach to Lamb-Wave Dispersion Curve Material Identification in Composite Plates. In Proceedings of the 10th European Workshop on Structural Health Monitoring (EWSHM), Palermo, Italy, 4–7 July 2022.
21. Golato, A.; Santhanam, S.; Ahmad, F.; Amin, M.G. Multimodal sparse reconstruction in guided wave imaging of defects in plates. *J. Electron. Imaging* **2016**, *25*, 043013. [CrossRef]
22. Yang, G.Y. Extraction and imaging research of Lamb wave single mode damage scattering wavefield. *Electron. Sci. Technol.* **2019**, *32*, 21–27.
23. Zhang, H.Y.; Duan, W.H. Defect detection of thin aluminum plate in frequency-wavenumber domain. *Acoust. Technol.* **2020**, *39*, 434–438.
24. Gorgin, R.; Wang, Z. Structural Damage Identification Based on Principal Curvatures of Mode Shape. *Int. J. Acoust. Vib.* **2021**, *25*, 566–576. [CrossRef]
25. Wang, Z.L.; Zhong, Y.; Zhou, J.; Li, C.; Zhong, L. Environmental Effects on Piezoelectric Sensors Array Signals and a Compensated Damage Imaging Method. *Materials* **2021**, *14*, 6742. [CrossRef] [PubMed]
26. Wang, B.; Shi, W.; Zhao, B.; Tan, J. A modal decomposition imaging algorithm for ultrasonic detection of delamination defects in carbon fiber composite plates using air-coupled Lamb waves. *Measurement* **2022**, *195*, 111165. [CrossRef]
27. Sang, S.; Sandgren, E. Study of in-plane wave propagation in 2-dimensional anisotropic elastic metamaterials. *J. Vib. Eng. Technol.* **2019**, *7*, 63–72. [CrossRef]
28. Wang, Z.; Fei, Y.; Li, B.; Zhou, A.; Gorgin, R. Research on the *f*-*k* Domain Multimodal Damage Detection Imaging Fusion Method in Metal Plate. *Trans. Indian Inst. Met.* **2022**, *75*, 2777–2786. [CrossRef]
29. Yue, F.E.I.; Wang, Z.P.; Ai, Z.H.O.U.; Li, B.Q. Research on Mode Superposition Damage Imaging Method for Isotropic Materials. In Proceedings of the 2020 15th Symposium on Piezoelectricity, Acoustic Waves and Device Applications (SPAWDA), Zhengzhou, China, 16–19 April 2021.
30. Wu, T.Y.; Ume, I.C. Fundamental study of laser generation of narrowband Lamb waves using superimposed line sources technique. *NDT E Int.* **2011**, *44*, 315–323. [CrossRef]
31. Joo, C.M.; Jaime, S.; Pereira, M. Stacking of multilayout and multichannel surface-wave data on the *f*-*k* domain. *J. Appl. Geophys.* **2018**, *159*, 93–107.